ADVANCED MATERIALS
www.advmat.de

Dynamic Control of Asymmetric Charge Distribution for Electrocatalytic Urea Synthesis

Xin Zhang, Hao Sun, Yi-Rong Wang, Zhan Shi, Rong-Lin Zhong, Chun-Yi Sun, Jing-Yao Liu, Zhong-Min Su,* and Ya-Qian Lan**

Constructing dual catalytic sites with charge density differences is an efficient way to promote urea electrosynthesis from parallel NO_3^- and CO_2 reduction yet still challenging in static system. Herein, a dynamic system is constructed by precisely controlling the asymmetric charge density distribution in an Au-doped coplanar Cu_7 clusters-based 3D framework catalyst (Au@cpCu_7CF). In Au@cpCu_7CF, the redistributed charge between Au and Cu atoms changed periodically with the application of pulse potentials switching between −0.2 and −0.6 V and greatly facilitated the electrosynthesis of urea. Compared with the static condition of pristine cpCu_7CF (FE_{urea} = 5.10%), the FE_{urea} of Au@cpCu_7CF under pulsed potentials is up to 55.53%. Theoretical calculations demonstrated that the high potential of −0.6 V improved the adsorption of $^*HNO_2$ and $^*NH_2$ on Au atoms and inhibited the reaction pathways of by-products. While at the low potential of −0.2 V, the charge distribution between Au and Cu atomic sites facilitated the thermodynamic C–N coupling step. This work demonstrated the important role of asymmetric charge distribution under dynamic regulation for urea electrosynthesis, providing a new inspiration for precise control of electrocatalysis.

1. Introduction

Electrocatalytic urea production by co-reduction of carbon dioxide (CO_2) and nitrate (NO_3^-) with renewable energy is a dual-goal strategy to replace the traditional industrial Bosch–Meiser process and eliminate environmental pollutants.[1] The electrosynthesis of urea is a typical C–N coupling reaction, and the rate-determining step requires specific C-specie and N-specie to form C–N bonds. Due to the competition of the parallel NO_3^- reduction reaction (NO_3RR) and CO_2 reduction reaction (CO_2RR), the co-reduction preferred urea pathway is inhibited, resulting in the undesirable selectivity. Researchers usually design dual-site catalysts that can catalyze CO_2RR and NO_3RR separately to match C–N coupling, as illustrated in Table S1 (Supporting Information).[2] For example, Li's team designed a Cu–W bimetallic oxide catalyst with alternating bimetallic reaction sites, which effectively improved the formation and coverage of $^*NO_2$ and $^*CO$ intermediates on WO_3 and CuO_X surface, respectively. Theoretical studies demonstrated that the combination of stable $^*NO_2$ and $^*CO$ intermediates increased the probability of C–N coupling and reduced the reaction energy barrier.[3] Zhang's team used amorphous iron and iron oxide nanoparticles as dual active sites to adsorb and activate of NO_3^- and CO_2, respectively. The subsequently generated key $^*NH_2$ and $^*CO$ intermediates were used for C–N coupling, which improved the efficiency of urea production.[2b] In general, a pair of effective catalytic active sites are designed to meet the needs for the key C–N coupling step. However, reactions involved in urea generation contain multiple continuous steps, each with unique energy and time characteristics. From this perspective, it is impossible for an active center to simultaneously promote both product desorption and reactant adsorption or surface reaction. Although direct efforts toward catalyst construction have achieved a significant contribution to electrocatalytic performance, optimizing multiple sequential reaction steps in the same catalytic system remains a challenging task.

Fortunately, a rational-designed dynamic catalytic system can theoretically provide the optimum condition for each reaction stage, enhancing the progress of the entire reaction sequence under ideal conditions.[4] It is feasible to finely tune the active sites to alternate among the ideal characteristics of product desorption, reactant adsorption, and surface reactions. Pulse technique has been regarded as a commonly used means for constructing dynamic electrocatalytic systems.[5] Compared to conventional

X. Zhang, H. Sun, Z. Shi, R.-L. Zhong, J.-Y. Liu, Z.-M. Su
State Key Laboratory of Supramolecular Structure and Materials
Institute of Theoretical Chemistry
College of Chemistry
Jilin University
Changchun, Jilin 130024, P. R. China
E-mail: ljy121@jlu.edu.cn; suzhongmin@jlu.edu.cn
Y.-R. Wang, Y.-Q. Lan
Guangdong Provincial Key Laboratory of Carbon Dioxide Resource Utilization School of Chemistry
South China Normal University
Guangzhou 510006, P. R. China
E-mail: yqlan@m.scnu.edu.cn
C.-Y. Sun
Key Laboratory of Polyoxometalate and Reticular Material Chemistry of Ministry of Education
Department of Chemistry
Northeast Normal University
Changchun, Jilin 130024, P. R. China
The ORCID identification number(s) for the author(s) of this article can be found under https://doi.org/10.1002/adma.202408510

DOI: 10.1002/adma.202408510

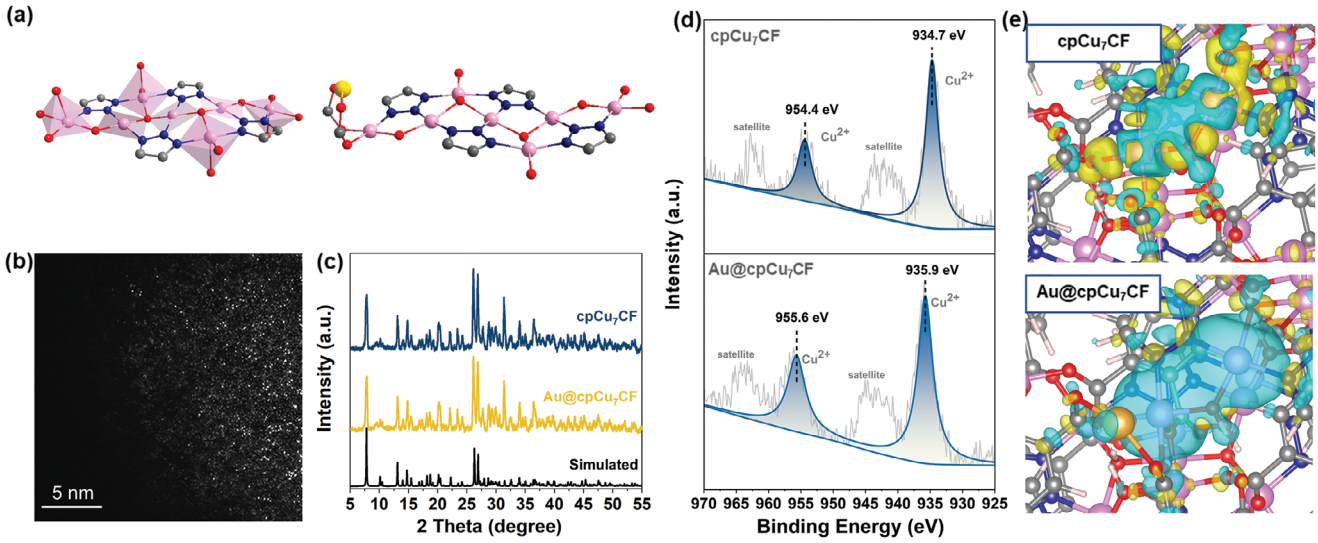

Figure 1. a) The secondary building unit of $cpCu_7CF$ (left) and $Au@cpCu_7CF$ (right). Among them, pink, blue, gray, red, and gold balls represented Cu, N, C, O, and Au atoms respectively. b) The HAADF-STEM morphology of $Au@cpCu_7CF$. c) XRD patterns of $cpCu_7CF$ and $Au@cpCu_7CF$. d) XPS pattern and e) charge density difference between $cpCu_7CF$ and $Au@cpCu_7CF$ (isosurface value: 0.001 e $Å^{-3}$). The yellow and cyan areas in the charge density difference plot represent electron accumulation and depletion, respectively.

static condition, the pulse-controlled dynamic catalytic paradigm requires the adoption of a new strategy in the time dimension. By programming the parameters of the pulse sequence, it is possible to specifically tailor the dominant products and improve the selectivity of the particular products.[6] Recently, He's team introduced pulse technology to the electrosynthesis of urea system. Under dynamic conditions, the local concentration of feedstock and key intermediates was effectively increased compared with static system, achieving excellent urea selectivity.[7] It is widely accepted that the thermodynamic process of electrocatalytic synthesis of urea is very sensitive to the charge density of the active sites.[8]

Here we constructed a dynamic system that can precisely control the charge density distribution of the catalytic sites for the efficient synthesis of urea. Au atoms were embedded in a coplanar Cu_7^{II} clusters-based 3D framework ($cpCu_7CF$) to break the original charge symmetry of $cpCu_7CF$ (named as $Au@cpCu_7CF$). Under dynamic conditions, the asymmetric charge distribution between Au and Cu atoms changed periodically with the pulse potential switching between −0.2 and −0.6 V versus the reversible hydrogen electrode (RHE). This dynamically controllable charge oscillation facilitated the efficient electrosynthesis of urea. Compared with the static condition of pristine $cpCu_7CF$ (FE_{urea} = 5.10%), the FE_{urea} of $Au@cpCu_7CF$ under pulsed potentials was up to 55.53%. Theoretical calculations demonstrated that the surface charge density of $Au@cpCu_7CF$ possessed a stronger response to the applied potentials compared with $cpCu_7CF$. When the potential switched to −0.6 V, Au atom with high charge density enhanced the immobilization of $^*HNO_2$ and $^*NH_2$ intermediates and inhibited the by-product pathways. While at the low potential of −0.2 V, the charge distribution between Au and Cu atom sites facilitated the thermodynamic C–N coupling step. Our work explored the important role of asymmetric charge distribution under dynamic regulation for urea electrosynthesis, providing a reference for the future investigation of dynamic electrocatalysis.

2. Results

2.1. Preparation and Characterization of the Electrocatalyst

Precisely control of the electron density on the active site of the catalyst can modulate the surface chemistry to achieve optimal rate and selectivity for the product.[9] Theoretical and experimental studies have demonstrated that breaking the symmetric charge distribution of the catalytic sites can effectively regulate the charge density, which is beneficial for reducing the energy barrier and improving the selectivity.[10] Considering the strong electron affinity of Au, we embedded Au atoms into the $cpCu_7CF$ constructed from coplanar Cu_7^{II} clusters to break the original charge symmetry. To account for the anchoring site of the Au atom, we considered seven positions including different surface carbonyl oxygen atoms, the hollow of triazole, and so on (Figure S1, Supporting Information). By comparing the binding energies of Au atoms anchored on different sites, Au atom was determined to be anchored on the surface carbonyl oxygen atoms near the Cu atom through the Au-O_2 coordination (**Figure 1a**). Additionally, the binding energy of −2.33 eV indicated that Au atom can stably locate at this site without agglomeration. High-angle annular dark-field scanning transmission electron microscope (HAADF-STEM) morphology displayed the single atom state of Au (Figure 1b). The morphology and HAADF-TEM-EDS mapping images of $Au@cpCu_7CF$ are shown in Figure S2 (Supporting Information). The X-ray diffraction (XRD) patterns of $cpCu_7CF$ and $Au@cpCu_7CF$ displayed that no metallic crystal diffraction peaks were detected, evidencing the absence of Au particles on $Au@cpCu_7CF$ (Figure 1c). X-ray photoelectron spectroscopy (XPS) and Cu LMM spectra demonstrated that the

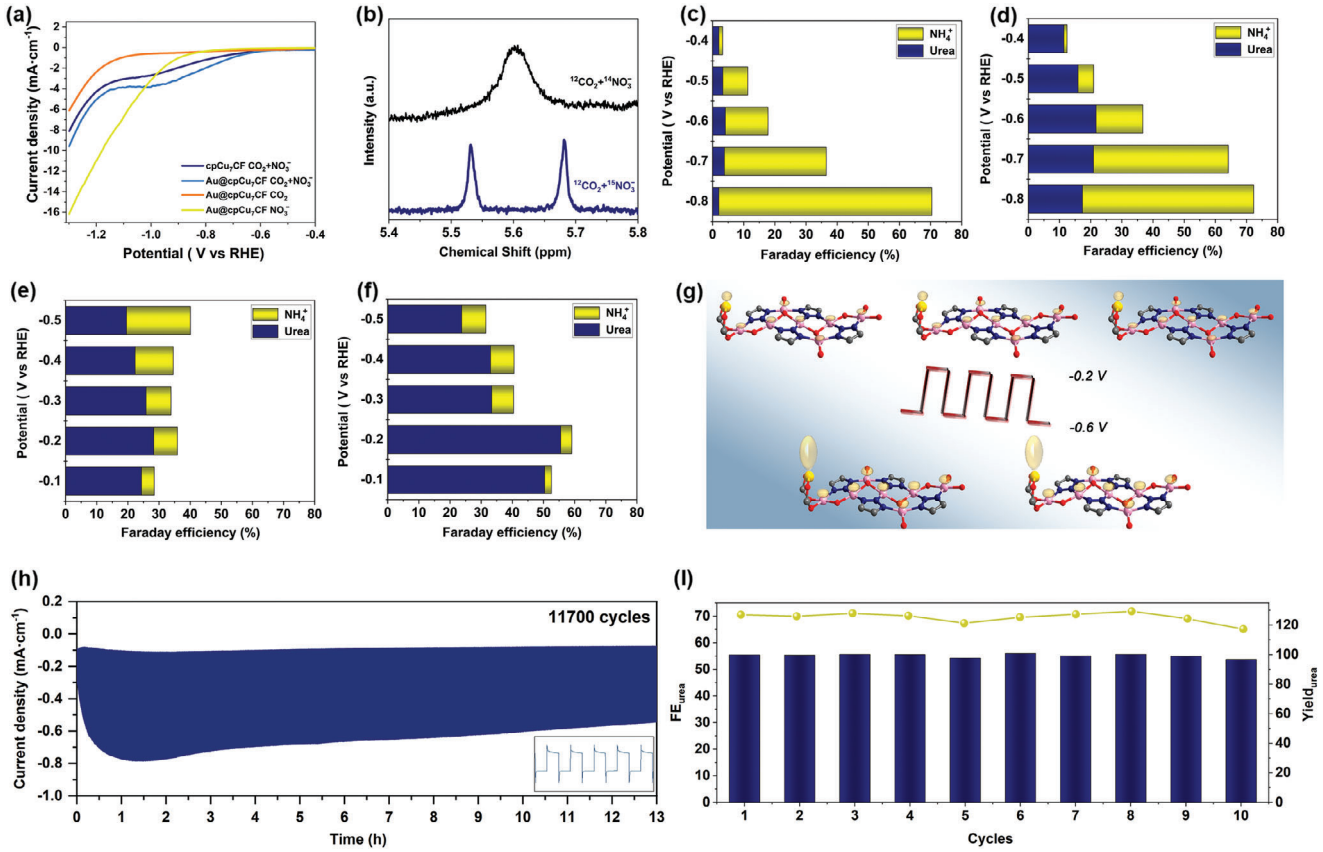

Figure 2. a) LSV curves for $cpCu_7CF$ and $Au@cpCu_7CF$. b) ^1H-NMR spectrum of $^{15}NH_2CO^{15}NH_2$ and $^{14}NH_2CO^{14}NH_2$. Faradaic efficiency on c) $cpCu_7CF$ and d) $Au@cpCu_7CF$ under constant potential conditions. Variation of Faraday efficiency with Ea on e) $cpCu_7CF$ and f) $Au@cpCu_7CF$ under pulsed conditions. The Ec was set to −0.6 V (vs RHE), and the ta and tc were all set to 2 s. All the C–N coupling reactions were carried out in 8 mM KNO_3 + 0.2 M K_2SO_4 solution saturated with CO_2. g) Schematic representation of surface charge variation with pulse potential on $Au@cpCu_7CF$. h) Stability of the $Au@cpCu_7CF$ under pulsed condition for 11 700 periods. i) Urea yields and FE for 10 cycles on $Au@cpCu_7CF$.

insertion of Au did not change the valence of Cu(II) (Figure 1d; Figure S3, Supporting Information). Furthermore, the Cu2p XPS signal of $Au@cpCu_7CF$ shifted to a higher binding energy by 1.2 eV compared to $cpCu_7CF$, indicating that the charge of Cu(II) migrated toward Au.[11] The theoretical charge density difference plot results showed that the introduction of Au caused a decrease in charge on adjacent copper atoms, which was consistent with the XPS characterization, suggesting that Au induced the charge redistribution (Figure 1e).

2.2. Performance of Urea Electrosynthesis

The electrochemical performance of $Au@cpCu_7CF$ for the CO_2RR, NO_3RR, and CO_2/NO_3^- co-reduction was evaluated in neutral media. Linear sweep voltammetry (LSV) curves indicated that $Au@cpCu_7CF$ exhibited stronger activity than $cpCu_7CF$ in CO_2/NO_3^- co-reduction, and their C–N coupling onset potentials were lower than that of CO_2RR or NO_3RR alone (**Figure 2a**). The C–N coupling on $cpCu_7CF$ and $Au@cpCu_7CF$ had a higher current density than CO_2RR and NO_3RR at lower potentials. At higher potential, the NO_3RR activity of $Au@cpCu_7CF$ was very high, which was related to its excellent NH_3 production capability (Figure S4, Supporting Information). Diacetylmonoxime method and urease decomposition colorimetric method were used to determine the content of urea (Figures S5, S6, Supporting Information). The isotope-labeling experiments results identified the formation of $^{14}NH_2CO^{14}NH_2$ and $^{15}NH_2CO^{15}NH_2$ products (Figure 2b). The indophenol blue method and naphthylenediamine hydrochloride method were used to determine the content of NH_4^+ and NO_2^-, respectively (Figures S6, S7, Supporting Information).

Under static conditions, the urea performance of $cpCu_7CF$ varied with potentials is shown in Figure 2c. At −0.6 V, the highest FE_{urea} was 5.10%. The introduction of Au improved the performance of urea, with a maximum FE_{urea} of 21.73% (Figure 2d). The introduced Au not only provided novel catalytic sites, but also crucially induced local charge asymmetry by disturbing the equilibrium of charge distribution on the planar $cpCu_7CF$ surface. Previous studies have indicated that this asymmetric charge distribution played a pivotal role in improving intermediate adsorption and reducing the C–N coupling barrier.[1a,8a,12] After applying a pulse potential, the optimal FE_{urea} of $Au@cpCu_7CF$ significantly reached up to 55.53% (Figure 2f). That was to say, the asymmetric charge distribution under dynamic conditions was more conducive to improving the selectivity of urea compared

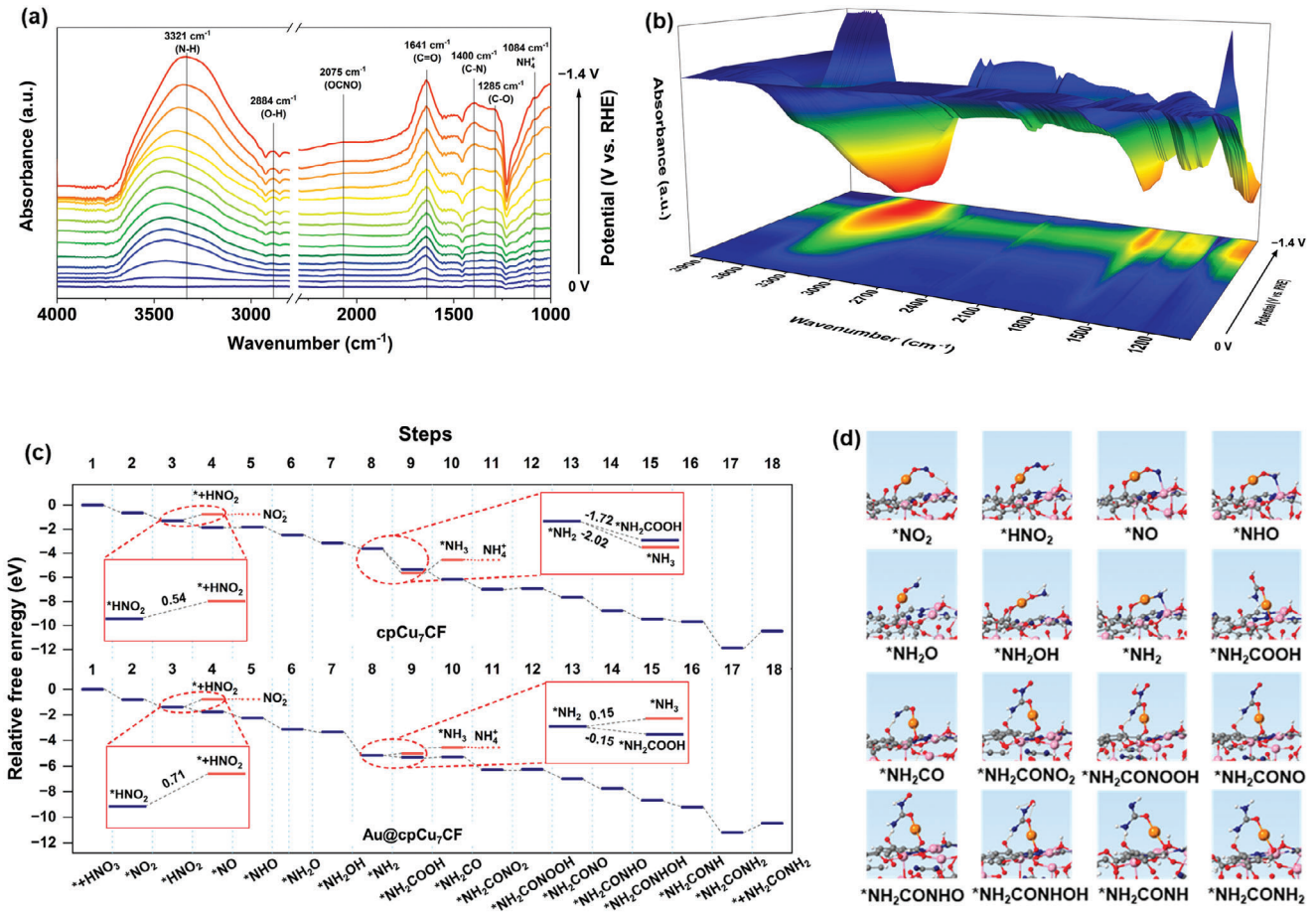

Figure 3. a) Operando SR-FTIR spectroscopy measurements under various potentials for Au@cpCu$_7$CF. b) 3D Operando SR-FTIR spectra of Au@cpCu$_7$CF in the range of 1000–4000 cm^{-1}. c) Free energy profiles of electroreduction of CO_2 and NO_3^- to urea on cpCu$_7$CF and Au@cpCu$_7$CF at 0 V. d) Structures of corresponding intermediates for urea production on Au@cpCu$_7$CF. The orange, pink, blue, red, gray, and white balls represented Au, Cu, N, O, C, and H atoms, respectively.

with static conditions. In contrast, the optimal FE_{urea} of cpCu$_7$CF with symmetrical charge distribution only reached 27.78% even under pulse conditions (Figure 2e). Besides, the effect of pulse period was explored (Figure S8, Supporting Information). Fixing cathodic potential (Ec) = −0.6 V and anode potential (Ea) = −0.2 V, the urea selectivity was promoted by applied dynamic pulse periods variations from 2 to 40 s. The optimal condition of pulse period was ta = tc = 2 s. Therefore, when the asymmetric charge on Au@cpCu$_7$CF exhibited dynamic oscillation, the C–N coupling pathway was facilitated (Figure 2g). The optimal $Yield_{urea}$ of Au@cpCu$_7$CF under dynamic conditions was 125.70 mg g^{-1} h^{-1}, which was six times as much as that of static cpCu$_7$CF (Figure S9, Supporting Information). Under the determined optimal pulsed conditions, Au@cpCu$_7$CF was able to maintain urea-producing performance over ten cycles and operated stably for 11 700 pulse periods (Figure 2i,h).

The CO_2RR and NO_3RR performance of Au@cpCu$_7$CF was shown in Figures S10, S11 (Supporting Information). Pulsing did not enhance the CO_2RR performance of Au@cpCu$_7$CF compared to static conditions. For NO_3RR, pulsed electrolysis under Ar atmosphere provided less FE_{NH3} due to the large amount of incompletely reduced intermediates generated at low negative potentials, which was unfavorable for the generation of the by-product NH_3. However, under CO_2/NO_3^- co-reduction, these incomplete reduction intermediates can serve as key species for C–N coupling with CO_2.[1b,2b,3,13] We also tested the CO_2RR and NO_3RR performance of cpCu$_7$CF under static and dynamic conditions respectively, and the trends were consistent with Au@cpCu$_7$CF. (Figures S12, S13, Supporting Information) As shown in Figure S14 (Supporting Information), cpCu7CF was able to maintain stability for 11 700 pulse periods.

2.3. Reaction Pathway of Urea Electrosynthesis

Operando SR-FTIR was performed on the Au@cpCu$_7$CF to track the evolution of reaction intermediates during the process of urea generation (**Figure 3**a,b). The infrared signals were collected from 1000 to 4000 cm^{-1} at a potential range of 0–−1.4 V versus RHE. The results showed that the intensity of the N–H peak at 3321 cm^{-1} gradually increased with the negative shift of the applied potential, signifying the formation of $^*NH_2$ intermediates originating from the NO_3RR.[1b] It should be noted that an

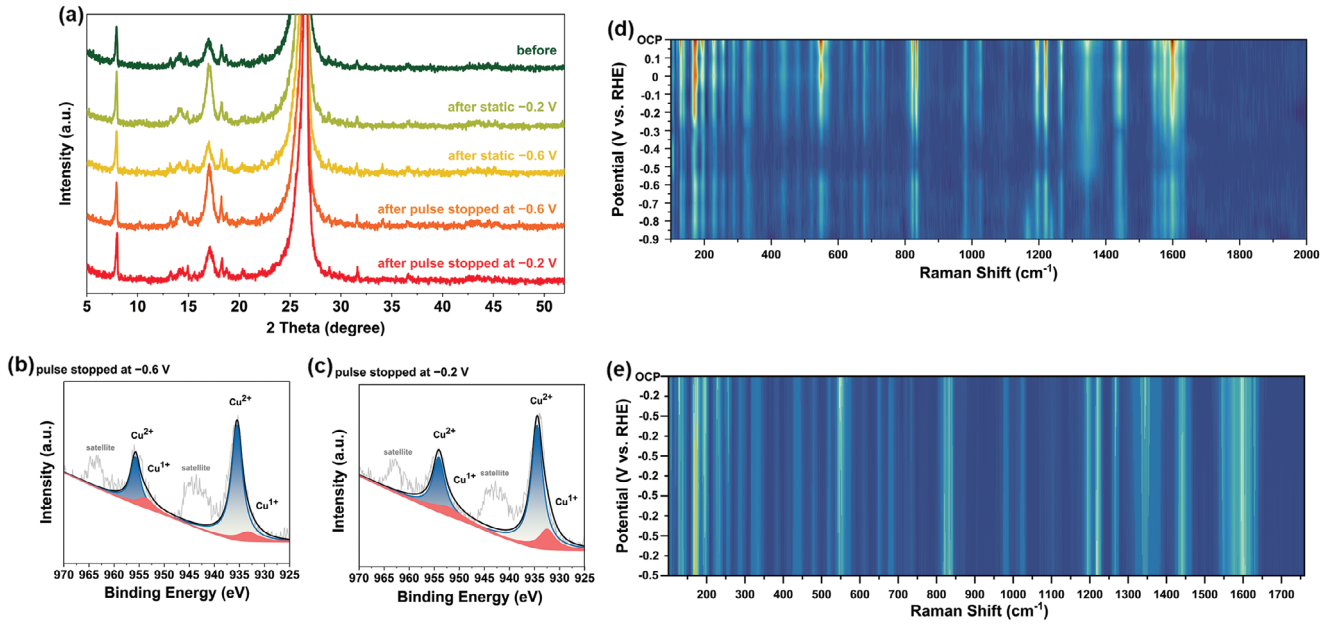

Figure 4. a) XRD comparison of Au@cpCu$_7$CF before and after 2 h electrolysis. XPS spectra of Au@cpCu$_7$CF after 2 h electrolysis under the pulsed condition with potential sequence stopped at b) Ec and c) Ea. In situ Raman spectra for Au@cpCu$_7$CF under d) constant potential condition and e) pulsed cycling.

obvious peak at 1400 and 2075 cm^{-1} corresponded to the C–N vibration bands and *OCNO, respectively.[1b,2a,c,13a,14]

Density functional theory (DFT) calculations were employed to further elucidate the reaction mechanism and the origin of catalytic activity (according to Figure 3a; Figure S15, Supporting Information). As shown in Figure 3c, the reaction started with the hydrogenation and dehydration steps leading to the formation of $^*HNO_2$. $^*HNO_2$ can be further reduced to $^*NO$ or evolved to release NO_2^-. Then, $^*NO$ underwent a series of hydrogenation and dehydration reactions to form $^*NH_2$. From here, two pathways emerged: $^*NH_2$ can be reduced to $^*NH_3$, which was then converted to NH_4^+, or participated in proton-coupled-electron-transfer (PCET) assisted C–N coupling to form $^*NH_2COOH$. This pathway of C–N coupling was consistent with the mechanism reported previously.[15] $^*NH_2COOH$ was then further hydrogenated and dehydrated to form $^*NH_2CO$, which led to $^*NH_2CONO_2$ through the second C–N coupling. And $^*NH_2CONO_2$ was converted to urea through successive reduction and dehydration steps. The structures of corresponding intermediates on cpCu$_7$CF and Au@cpCu$_7$CF were depicted in Figure S16 (Supporting Information) and Figure 3d. The results show that the formation of the NO_2^- byproduct depended on the desorption of HNO_2, while the formation of NH_4^+ depended on the competition between the hydrogenation of $^*NH_2$ and PCET-assisted C–N coupling. Furthermore, free energy diagrams at 0 V indicated that Au@cpCu$_7$CF suppressed the desorption of HNO_2 with a higher desorption energy (0.71 eV) than cpCu$_7$CF (0.54 eV). Additionally, $^*NH_2$ to $^*NH_2COOH$ became more thermodynamically favorable after the introduction of Au. Hence, the incorporation of Au inhibited the production of by-products, improving the pathway for urea synthesis.

2.4. Dynamic Regulation Mechanism of Asymmetric Charge Distribution

Numerous excellent studies have applied pulse techniques to enhance electrocatalytic performance. These researches can be roughly divided into the following two aspects. One aspect referred to the potential-dependent dynamic transformation of the catalyst, which enabled the active sites to regenerate continuously.[6a,16] For example, Cuenya's team tuned the surface structure and composition of the Cu catalyst by rational designing the applied pulse potential sequence.[5b] For the other situation, the structure of the catalyst was constantly stable during the duration of the pulse, but the changes in surface microenvironment influenced adsorbed species and intermediates.[7,17] In order to explore the micro-mechanism of dynamic pulse in this work, the XRD of Au@cpCu$_7$CF before and after the reaction was tested. As shown in **Figure** 4a, the crystalline phase of Au@cpCu$_7$CF remained stable after static and pulsed electrolysis for 2 h, and no formation of Cu(0) was detected. Figure 4b,c shows the XPS of Au@cpCu$_7$CF after the pulse electrocatalysis. Compared with the static −0.2 and −0.6 V, a smaller amount of Cu(I) was generated after pulse electrolysis for 2 h (Figures S17, S18, Supporting Information). Thus, the pulsed condition was more favorable for keeping the composition and valence stable. Despite the inevitable formation of Cu(I), we still consider the initial structure as the active site. Because the higher amounts of Cu(I) were detrimental to urea production. Besides, the in situ Raman spectra of Au@cpCu$_7$CF were also measured to detect the structural changes during electrolysis (Figure 4d). The results shown that all chemical bonds were retained and no new peaks appeared as the applied potential increased from open circuit potential (OCP) to −0.6 V, indicating the Au@cpCu$_7$CF

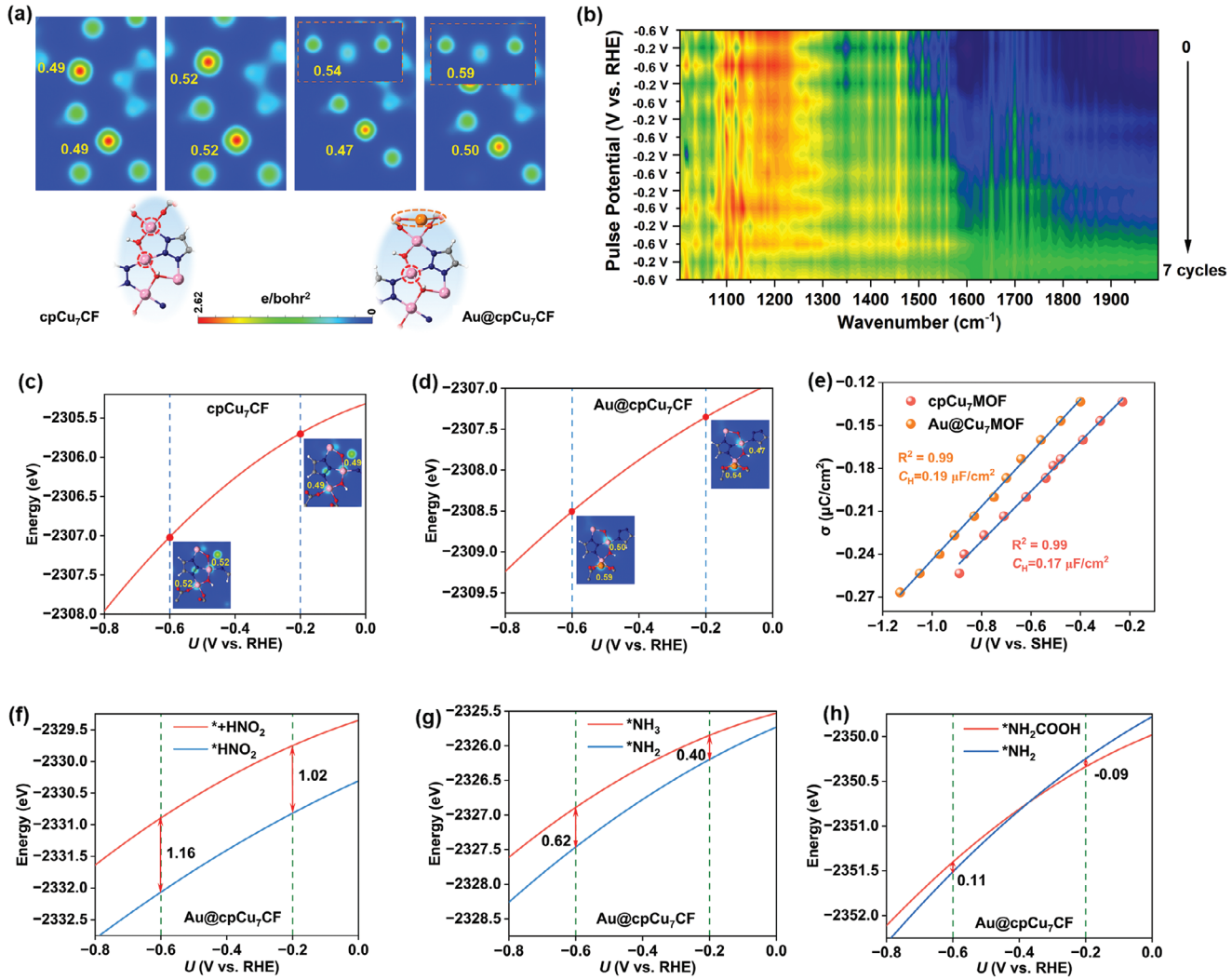

Figure 5. a) 2D slices of charge density plots for $cpCu_7CF$ and $Au@cpCu_7CF$ at −0.2 and −0.6 V. b) Operando SR-FTIR of $Au@cpCu_7CF$ under pulsed cycling. Energies of c) $cpCu_7CF$ and d) $Au@cpCu_7CF$ as a function of applied potentials. e) Differential Helmholtz capacitances of $cpCu_7CF$ and $Au@cpCu_7CF$. Energies of f) $^*HNO_2$ and $^*+HNO_2$, g) $^*NH_2$ and $^*NH_3$, and h) $^*NH_2$ and $^*NH_2COOH$ on $Au@cpCu_7CF$ as a function of applied potentials.

remained stable structure. When the voltage reached −0.7 V, new chemical bonds were formed at 1167 and 1240 cm^{-1}, respectively. That is, when the voltage exceeded the threshold of −0.7 V, the structure of $Au@cpCu_7CF$ underwent a small reconstruction even though the main framework was still maintained. As shown in Figure 4e, $Au@cpCu_7CF$ maintained stability when the pulse potential was switched between −0.2 and −0.6 V, demonstrating that the structure and composition of $Au@cpCu_7CF$ did not dynamically transform by pulse potential in this work. Therefore, the improvement of urea performance under dynamic conditions can be attributed to the second scenario mentioned above, where potential disturbance affected the adsorbed species and intermediates. In addition, we also measured the XRD patterns, in situ Raman spectra, and Cu XPS signal of $cpCu_7CF$ before and after the reaction. The trend was consistent with $Au@cpCu_7CF$ (Figures S19–S23, Supporting Information).

To further account for the influence of pulse potential, the energy and electron distribution of pristine catalysts and key intermediates under work conditions (U = −0.2 and −0.6 V vs RHE, pH 5) were calculated using the constant-potential model (CPM). For the $cpCu_7CF$, the charge density at the two Cu sites was uniformly distributed and increased proportionally with the applied potential. As shown in **Figure 5a**, the charge density at Cu sites both increased from 0.49 to 0.52 e $bohr^{-2}$ as the applied potential switched from −0.2 to −0.6 V. The introduction of Au induced the charge rearrangement, with the charge migrating from the Cu atom to Au atom for $Au@cpCu_7CF$ (as shown in Cu2p XPS signal and charge density difference plot in Figure 1d,e). When the potential was −0.2 V, the charge density of Au and Cu was 0.54 and 0.47 e $bohr^{-2}$, respectively. The degree of the asymmetric charge distribution between Au and Cu increased further when the potential switched to −0.6 V. And the charge density of Au and Cu was converted to 0.59 and 0.50 e $bohr^{-2}$, respectively. The surface

charge density of Au responded more strongly to the applied potential, which was attributed to the larger differential Helmholtz capacitance ($C_H = d\sigma/dU$) for Au@cpCu$_7$CF (0.19 μF cm^{-2}) compared to cpCu$_7$CF (0.17 μF cm^{-2}). (Figure 5c–e) When the pulse potential dynamically switched between −0.2 and −0.6 V, we considered that the surface charge density of Au@cpCu$_7$CF showed a remarkable periodical asymmetric fluctuation. The operando SR-FTIR of Au@cpCu$_7$CF under pulsed conditions was measured and the result shown that the dynamically controllable charge asymmetry oscillation induced a periodic cycling of the active species (Figure 5b). In contrast, the symmetric charge distribution of cpCu$_7$CF did not have such an impact under dynamic conditions (Figure S24, Supporting Information).

Given the distinct binding energies of surface species, it is known that precise control over the competition among concurrent catalytic surface reactions can be exercised under dynamic conditions.[17c,18] Here we calculated the ΔG values of the key elementary steps at both −0.2 and −0.6 V to assess the influence of the pulse potential on the reaction process. The corresponding calculated results are listed in Table S2 (Supporting Information). Figure 5f demonstrated that at −0.6 V, Au@cpCu$_7$CF exhibited an increased desorption energy of HNO_2 (1.16 eV) compared to that at −0.2 V (1.02 eV), indicating a more effective suppression of the NO_2^- byproduct formation at a higher potential. As displayed in Figure 5g, the ΔG for $^*NH_2$ reduction to $^*NH_3$ on Au@cpCu$_7$CF was higher at −0.6 V than at −0.2 V (0.62 vs 0.40 eV), indicating that −0.6 V was also conducive to inhibiting the formation of NH_4^+ byproduct. The high charge density on Au at −0.6 V stabilized the key $^*HNO_2$ and $^*NH_2$ intermediates and suppressed the side reactions, contributing to the urea formation pathway. Compared to $^*NH_2$ hydrogenation, the conversion of $^*NH_2$ to $^*NH_2COOH$ had a positive ΔG of at −0.6 V (0.11 eV) and a negative ΔG at −0.2 V (−0.09 eV), as depicted in Figure 5h. This result implied that −0.2 V was superior for the C–N coupling in thermodynamic perspective. As a result, the pulse potential can be dynamically switched between optimal conditions for fixed key intermediates (−0.6 V) and thermodynamically optimal conditions for C–N coupling (−0.2 V), achieving maximal urea selectivity. For cpCu$_7$CF, $^*NH_2$ conversion to $^*NH_2COOH$ was also better at −0.2 V than −0.6 V (Figure S25, Supporting Information). However, the cpCu$_7$CF exhibited less inhibition of byproduct formation (Figure S26, Supporting Information).

Overall, the thermodynamic process of urea synthesis was very sensitive to the charge density of the catalytic sites. The introduction of Au broke the state of symmetric charge distribution among the pristine cpCu$_7$CF sites. And the degree of charge asymmetry distribution between Au and Cu was modulated by the applied potential. Theoretical calculations showed that Au with high charge density was beneficial for immobilizing $^*HNO_2$ and $^*NH_2$ intermediates than that of Cu, while the Au–Cu charge distribution at −0.2 V was more favorable for the thermodynamic C–N coupling step. Thus, the thermodynamic pathways can be dynamically switched by pulse potential, which was conducive to the high performance for urea formation.

3. Conclusion

In conclusion, we demonstrated a dynamic control of charge distribution on electrocatalysts to better regulate the multiple steps of sequential reactions in urea electrosynthesis. By embedding Au single-atom in an intriguing 3D framework constructed from coplanar Cu_7^{II} clusters, the charge on metals was rearranged and the original charge symmetry was broken. On this basis, a dynamic pulse potential was applied to further strengthen asymmetric charge distribution. It was found that the charge density of Au atoms had a strong response to the applied potential. Therefore, when the pulse potential was dynamically switched between −0.2 and −0.6 V, the asymmetric charge distribution between Au and Cu atom changed periodically. Theoretical calculations demonstrated that the pulse potentials enable the reaction system to switch dynamically between the optimal conditions for fixing the key $^*HNO_2$ and $^*NH_2$ intermediates (−0.6 V) and the thermodynamically optimal conditions for C–N coupling (−0.2 V). Under this dynamically controllable charge oscillation, the highest equilibrium point of urea-selective performance was achieved. Compared with the static condition of pristine cpCu$_7$CF (FE_{urea} = 5.10%), the FE_{urea} of Au@cpCu$_7$CF under pulsed potentials was up to 55.53%. These findings demonstrated the dynamic asymmetric charge distribution induced by pulsed potential and the intrinsic origin of enhanced urea selectivity, opening an avenue for rational design and precise control of dynamic electrocatalysis progress.

Supporting Information

Supporting Information is available from the Wiley Online Library or from the author.

Acknowledgements

X.Z. and H.S. contributed equally to this work. This work was financially supported by the National Natural Science Foundation of China (Grant No. 22271023).

Conflict of Interest

The authors declare no conflict of interest.

Data Availability Statement

The data that support the findings of this study are available from the corresponding author upon reasonable request.

Keywords

asymmetric charge density distribution, dynamic catalytic system, electrosynthesis of urea, precisely control

Received: June 15, 2024
Revised: July 22, 2024
Published online:

[1] a) N. Meng, X. Ma, C. Wang, Y. Wang, R. Yang, J. Shao, Y. Huang, Y. Xu, B. Zhang, Y. Yu, *ACS Nano* **2022**, *16*, 9095; b) C. Lv, L. Zhong, H. Liu, Z. Fang, C. Yan, M. Chen, Y. Kong, C. Lee, D. Liu, S. Li, J. Liu, L. Song, G. Chen, Q. Yan, G. Yu, *Nat. Sustain.* **2021**, *4*, 868; c) N. Li, H. Gao, Z. Liu, Q. Zhi, B. Li, L. Gong, B. Chen, T. Yang, K. Wang, P. Jin, J. Jiang, *Sci. China Chem.* **2023**, *66*, 1417.

[2] a) M. Qiu, X. Zhu, S. Bo, K. Cheng, N. He, K. Gu, D. Song, C. Chen, X. Wei, D. Wang, Y. Liu, S. Li, X. Tu, Y. Li, Q. Liu, C. Li, S. Wang, *CCS Chem.* **2023**, *5*, 2617; b) J. Geng, S. Ji, M. Jin, C. Zhang, M. Xu, G. Wang, C. Liang, H. Zhang, *Angew. Chem., Int. Ed.* **2023**, *62*, 202210958; c) C. Chen, S. Li, X. Zhu, S. Bo, K. Cheng, N. He, M. Qiu, C. Xie, D. Song, Y. Liu, W. Chen, Y. Li, Q. Liu, C. Li, S. Wang, *Carbon Energy* **2023**, *5*, e345.

[3] Y. Zhao, Y. Ding, W. Li, C. Liu, Y. Li, Z. Zhao, Y. Shan, F. Li, L. Sun, F. Li, *Nat. Commun.* **2023**, *14*, 4491.

[4] M. A. Ardagh, O. A. Abdelrahman, P. J. Dauenhauer, *ACS Catal.* **2019**, *9*, 6929.

[5] a) R. Casebolt, K. Levine, J. Suntivich, T. Hanrath, *Joule* **2021**, *5*, 1987; b) R. M. Arán-Ais, F. Scholten, S. Kunze, R. Rizo, B. R. Cuenya, *Nat. Energy* **2020**, *5*, 317; c) Z. Li, L. Wang, T. Wang, L. Sun, W. Yang, *J. Am. Chem. Soc.* **2023**, *145*, 20655.

[6] a) J. Timoshenko, A. Bergmann, C. Rettenmaier, A. Herzog, R. M. Arán-Ais, H. S. Jeon, F. T. Haase, U. Hejral, P. Grosse, S. Kühl, E. M. Davis, J. Tian, O. Magnussen, B. R. Cuenya, *Nat. Catal.* **2022**, *5*, 259; b) X.-D. Zhang, T. Liu, C. Liu, D.-S. Zheng, J.-M. Huang, Q.-W. Liu, W.-W. Yuan, Y. Yin, L.-R. Huang, M. Xu, Y. Li, Z.-Y. Gu, *J. Am. Chem. Soc.* **2023**, *145*, 2195.

[7] Q. Hu, W. Zhou, S. Qi, Q. Huo, X. Li, M. Lv, X. Chen, C. Feng, J. Yu, X. Chai, H. Yang, C. He, *Nat. Sustain.* **2024**, *7*, 442.

[8] a) C. Lv, C. Lee, L. Zhong, H. Liu, J. Liu, L. Yang, C. Yan, W. Yu, H. H. Hng, Z. Qi, L. Song, S. Li, K. P. Loh, Q. Yan, G. Yu, *ACS Nano* **2022**, *16*, 8213; b) Q. Zhao, X. Lu, Y. Wang, S. Zhu, Y. Liu, F. Xiao, S. X. Dou, W.-H. Lai, M. Shao, *Angew. Chem., Int. Ed.* **2023**, *62*, 202307123; c) Y. Liu, X. Tu, X. Wei, D. Wang, X. Zhang, W. Chen, C. Chen, S. Wang, *Angew. Chem., Int. Ed.* **2023**, *62*, 202300387.

[9] a) L. Tao, M. Qiao, R. Jin, Y. Li, Z. Xiao, Y. Wang, N. Zhang, C. Xie, Q. He, D. Jiang, G. Yu, Y. Li, S. Wang, *Angew. Chem., Int. Ed.* **2019**, *58*, 1019; b) S. Dai, J.-P. Chou, K.-W. Wang, Y.-Y. Hsu, A. Hu, X. Pan, T.-Y. Chen, *Nat. Commun.* **2019**, *10*, 440; c) X. Peng, M. Zhang, H. Qin, J. Han, Y. Xu, W. Li, X.-P. Zhang, W. Zhang, U.-P. Apfel, R. Cao, *Angew. Chem., Int. Ed.* **2024**, *63*, 202401074; d) L. Sun, C. Dai, T. Wang, X. Jin, Z. J. Xu, X. Wang, *Angew. Chem., Int. Ed.* **2024**, *63*, 202320027.

[10] L. Liang, L. Yang, T. Heine, A. Arinchtein, X. Wang, J. Hübner, J. Schmidt, A. Thomas, P. Strasser, *Adv. Energy Mater.* **2024**, *14*, 2304224.

[11] a) Y. Zhang, B. Johannessen, P. Zhang, J. Gong, J. Ran, S.-Z. Qiao, *Adv. Mater.* **2023**, *35*, 2306923; b) M. Wang, X.-N. Ren, G. Yuan, X.-P. Niu, Q.-L. Xu, W.-L. Gao, S.-K. Zhu, Q.-F. Wang, *J. CO2 Util.* **2020**, *37*, 204.

[12] C. Chen, X. Zhu, X. Wen, Y. Zhou, L. Zhou, H. Li, L. Tao, Q. Li, S. Du, T. Liu, D. Yan, C. Xie, Y. Zou, Y. Wang, R. Chen, J. Huo, Y. Li, J. Cheng, H. Su, X. Zhao, W. Cheng, Q. Liu, H. Lin, J. Luo, J. Chen, M. Dong, K. Cheng, C. Li, S. Wang, *Nat. Chem.* **2020**, *12*, 717.

[13] a) X. Wei, Y. Liu, X. Zhu, S. Bo, L. Xiao, C. Chen, T. T. T. Nga, Y. He, M. Qiu, C. Xie, D. Wang, Q. Liu, F. Dong, C.-L. Dong, X.-Z. Fu, S. Wang, *Adv. Mater.* **2023**, *35*, 2300020; b) M. Sun, G. Wu, J. Jiang, Y. Yang, A. Du, L. Dai, X. Mao, Q. Qin, *Angew. Chem., Int. Ed.* **2023**, *62*, 202301957.

[14] a) X. Wei, X. Wen, Y. Liu, C. Chen, C. Xie, D. Wang, M. Qiu, N. He, P. Zhou, W. Chen, J. Cheng, H. Lin, J. Jia, X.-Z. Fu, S. Wang, *J. Am. Chem. Soc.* **2022**, *144*, 11530; b) D. Zhang, Y. Xue, X. Zheng, C. Zhang, Y. Li, *Natl. Sci. Rev.* **2023**, *10*, nwac209; c) H.-Q. Yin, Z.-S. Sun, Q.-P. Zhao, L.-L. Yang, T.-B. Lu, Z.-M. Zhang, *J. Energy Chem.* **2023**, *84*, 385.

[15] a) Q. Wu, C. Dai, F. Meng, Y. Jiao, Z. J. Xu, *Nat. Commun.* **2024**, *15*, 1095; b) X. Liu, J. Feng, X. Cheng, J. Zhang, J. Huo, D. Chen, A. Marcomini, Y. Li, Q. Xu, J. Lu, *Adv. Funct. Mater.* **2024**, 2400892; c) X. Huang, Y. Li, S. Xie, Q. Zhao, B. Zhang, Z. Zhang, H. Sheng, J. Zhao, *Angew. Chem., Int. Ed.* **2024**, *63*, 202403980.

[16] a) H. S. Jeon, J. Timoshenko, C. Rettenmaier, A. Herzog, A. Yoon, S. W. Chee, S. Oener, U. Hejral, F. T. Haase, B. R. Cuenya, *J. Am. Chem. Soc.* **2021**, *143*, 7578; b) W. Lai, Z. Ma, J. Zhang, Y. Yuan, Y. Qiao, H. Huang, *Adv. Funct. Mater.* **2022**, *32*, 2111193; c) K. W. Kimura, R. Casebolt, J. C. DaSilva, E. Kauffman, J. Kim, T. A. Dunbar, C. J. Pollock, J. Suntivich, T. Hanrath, *ACS Catal.* **2020**, *10*, 8632; d) S.-C. Lin, C.-C. Chang, S.-Y. Chiu, H.-T. Pai, T.-Y. Liao, C.-S. Hsu, W.-H. Chiang, M.-K. Tsai, H. M. Chen, *Nat. Commun.* **2020**, *11*, 3525.

[17] a) C. W. Lee, N. H. Cho, K. T. Nam, Y. J. Hwang, B. K. Min, *Nat. Commun.* **2019**, *10*, 3919; b) C. S. Le Duff, M. J. Lawrence, P. Rodriguez, *Angew. Chem., Int. Ed.* **2017**, *56*, 12919; c) J. C. Bui, C. Kim, A. Z. Weber, A. T. Bell, *ACS Energy Lett.* **2021**, *6*, 1181; d) R. C. DiDomenico, T. Hanrath, *ACS Energy Lett.* **2022**, *7*, 292.

[18] B. Kumar, J. P. Brian, V. Atla, S. Kumari, K. A. Bertram, R. T. White, J. M. Spurgeon, *ACS Catal.* **2016**, *6*, 4739.